저작자표시-동일조건변경허락 2.0 대한민국

이용자는 아래의 조건을 따르는 경우에 한하여 자유롭게

- 이 저작물을 복제, 배포, 전송, 전시, 공연 및 방송할 수 있습니다.
- 이차적 저작물을 작성할 수 있습니다.
- 이 저작물을 영리 목적으로 이용할 수 있습니다.

다음과 같은 조건을 따라야 합니다:

저작자표시. 귀하는 원저작자를 표시하여야 합니다.

동일조건변경허락. 귀하가 이 저작물을 개작, 변형 또는 가공했을 경우에는, 이 저작물과 동일한 이용허락조건하에서만 배포할 수 있습니다.

- 귀하는, 이 저작물의 재이용이나 배포의 경우, 이 저작물에 적용된 이용허락조건을 명확하게 나타내어야 합니다.
- 저작권자로부터 별도의 허가를 받으면 이러한 조건들은 적용되지 않습니다.

저작권법에 따른 이용자의 권리는 위의 내용에 의하여 영향을 받지 않습니다.

이것은 이용허락규약(Legal Code)을 이해하기 쉽게 요약한 것입니다.

Disclaimer

dCollection

[UCI]I804:24011-200000264546
조선대학교 CHOSUN UNIVERSITY

2015年 2月 碩士學位論文 Amorphous Indium Selenide Thin Films as a Buffer Layer for CIGS Solar Cells 유 명 한

2015年 2月

碩士學位 論文

Amorphous Indium Selenide Thin Films as a Buffer Layer for CIGS Solar Cells

朝鮮大學校 大學院

電氣工學科

유 명 한

조선대학교
CHOSUN UNIVERSITY

Amorphous Indium Selenide Thin Films as a Buffer Layer for CIGS Solar Cells

CIGS 태양전지용 비정질 인듐 셀레나이드 완충 박막

2015年 2月 25日

朝鮮大學校 大學院

電氣工學科

유 명 한

Collection @ chosun

조선대학교 CHOSUN UNIVERSITY

Amorphous Indium Selenide Thin Films as a Buffer Layer for CIGS Solar Cells

指導敎授　金 南 勳

이 論文을 工學碩士學位 申請論文으로 提出함.

2014年 10月

朝鮮大學校 大學院

電氣工學科

유 명 한

Collection @ chosun

조선대학교 CHOSUN UNIVERSITY

柳명한의 碩士學位論文을 認准함

委員長 朝鮮大學校 敎授 李 愚 宣 印

委 員 朝鮮大學校 敎授 曺 錦 培 印

委 員 朝鮮大學校 敎授 金 南 勳 印

2014年 11月

朝鮮大學校 大學院

Collection @ chosun

조선대학교
CHOSUN UNIVERSITY

Contents

ABSTRACT

Ⅰ. Introduction ········· 1

Ⅱ. Theoretical Background ········· 3

A. CIGS Thin Film Solar Cells ········· 3

1. Structure of CIGS Thin Film ········· 3

2. Characteristics of Buffer Layer for CIGS Solar Cells ········· 5

B. Principles of Sputtering ········· 8

1. RF Sputtering ········· 8

2. Magnetron Sputtering ········· 9

C. Principles of Annealing : Rapid Thermal Annealing (RTA) ········· 11

D. Analysis of Thin Film ········· 12

1. Field Emission Scanning Electron Microscope (FE-SEM) ········· 12

2. X-Ray Diffraction (XRD) ········· 12

3. Hall Effect Measurement System ········· 14

4. UV-Visible Spectrophotometer ········· 17

Collection @ chosun

조선대학교 CHOSUN UNIVERSITY

Ⅲ. Non-stoichiometric Amorphous Indium Selenide Thin Films ······ 19

A. Experimental Details ······ 19

B. Results and Discussion ······ 20

Ⅳ. Nano-scaled Thickness of Indium Selenide Thin Films as a Buffer Layer ······ 28

A. Experimental Details ······ 28

B. Results and Discussion ······ 29

Ⅵ. Conclusion ······ 36

Reference

Collection @ chosun

조선대학교 CHOSUN UNIVERSITY

List of Tables

Table 1. Process conditions in sputtering and annealing ················ 20
Table 2. Sputtering conditions for the adjustment of
the film thickness ·· 29

Collection @ chosun

조선대학교 CHOSUN UNIVERSITY

List of Figures

Fig. 1 Structure of CIGS solar cells used as a buffer layer to Indium Selenide ······ 3
Fig. 2 RF Sputtering Configuration ······ 9
Fig. 3 RF magnetron sputtering equipment (I.D.T. ENG) ······ 10
Fig. 4 Rapid Thermal Annealing equipment (GD Tech) ······ 11
Fig. 5 Principles of XRD analysis ······ 13
Fig. 6 XRD equipment (Philips X'pert-PRO-MRD XRD) ······ 13
Fig. 7 Schematic diagram of the Hall-effect Measurement ······ 15
Fig. 8 Hall Effect Measurement System equipment (Accent Optical Technologies. HL5500PC) ······ 16
Fig. 9 Diagram of UV-visible Spectroscopy ······ 17
Fig. 10 UV-visible Spectrophotometer equipment (Varian Techtron. Cary 500 scan) ······ 18
Fig. 11 FESEM images and XRD spectra of the (a) as-deposited and the RTA-treated indium selenide thin films at the annealing temperatures of (b) 400℃, (c) 500℃, (d) 600℃, and (e) 700℃ ······ 22
Fig. 12 EDX result for specimens of the (a) as-deposited and the RTA-treated indium selenide thin films at the annealing temperatures of (b) 400℃, (c) 500℃, (d) 600℃, and (e) 700℃ ······ 23
Fig. 13 Optical transmittance for specimens of the (a) as-deposited and the RTA-treated indium selenide thin films at the annealing temperatures of (b) 400℃, (c) 500℃, (d) 600℃, and (e) 700℃ ······ 24

Collection @ chosun

조선대학교 CHOSUN UNIVERSITY

Fig. 14 Band gap energy of the (a) as-deposited and the RTA-treated indium selenide thin films at the annealing temperatures of (b) 400℃, (c) 500℃, (d) 600℃, and (e) 700℃ ······ 25
Fig. 15 Resistivity, carrier concentration and carrier mobility of the (a) as-deposited and the RTA-treated indium selenide thin films at the annealing temperatures of (b) 400℃, (c) 500℃, (d) 600℃, and (e) 700℃ ······ 26
Fig. 16 XRD spectra of the indium selenide thin films at the different thickness of (a) 30, (b) 40, (c) 50, (d) 60, and (e) 70 nm ······ 30
Fig. 17 FESEM images and atomic percent of the indium selenide thin films at the different thickness of (a) 30, (b) 40, (c) 50, (d) 60, and (e) 70 nm ······ 31
Fig. 18 Optical transmittance of the indium selenide thin films at the different thickness of (a) 30, (b) 40, (c) 50, (d) 60, and (e) 70 nm ······ 34
Fig. 19 Band gap energy of the indium selenide thin films at the different thickness of (a) 30, (b) 40, (c) 50, (d) 60, and (e) 70 nm ······ 34
Fig. 20 Resistivity, carrier Concentration and carrier mobility of the indium selenide thin films at the different thickness of (a) 30, (b) 40, (c) 50, (d) 60, and (e) 70 nm ······ 35

Collection @ chosun

조선대학교 CHOSUN UNIVERSITY

ABSTRACT

CIGS 태양전지용 비정질 인듐 셀레나이드 완충 박막

Yoo, Myoung Han
Advisor : Prof. Kim, Nam-Hoon, Ph.D.
Department of Electrical Engineering
Graduate School of Chosun University

CIGS 태양전지는 적절한 광흡수, 전기적 안정성, 무 독성 등의 이유로 박막태양전지에서 유망한 재료이며, 갈륨과 인듐의 조성비를 조절함으로써 밴드갭의 조절이 가능하다는 장점이 있다. 일반적으로 CIGS 박막 태양전지는 유리기판/몰리브데늄(Mo)/CIGS 흡수층/완충막/투명전극 (transparent conductive oxide, TCO) 의 구조를 가진다.

카드뮴 설페이드 (CdS)는 기존의 CIGS 태양전지의 완충막으로 가장 널리 쓰이고 있다. 그러나 카드뮴 (Cd)은 인체나 환경에 매우 유해한 중금속이기 때문에 이를 대체하기 위한 대체 재료가 많이 연구되고 있다. 태양전지 산업에서 환경 재활용 비용을 줄이기 위해 카드뮴을 대체하기 위한 재료에는 징크 셀레나이드 (zinc selenide)와 인듐 셀레나이드 (indium selenide) 등이 있다. 인듐 셀레나이드는 직접 천이형 밴드갭을 갖는 III-VI 화합물로 전자, 광전자 및 태양전지에서 사용할 수 있는 유용한 특성을 가지고 있다. 인듐 셀레나이드는 넓은 범위의 밴드갭 조절 (1.1~3.5 eV)이 가능하며 CIGS 흡수층과 이종접합이 가능하기 때문에 CIGS 태양전지의 완충막으로서 적합하다. 인듐 셀레나이드는 비화학양론적인 In_xSe_y의 공존과 화학양론적인 $InSe$, In_2Se_3, In_4Se_3, In_5Se_7, In_6Se_7, In_9Se_{11}의 서로간 근접한 형성온도 때문에 화학양론적으로 조절하는 것이 매우 힘들다. 인듐 셀레나이드의 구조적, 광 및 전기적 특성은 증착공정 및 포스트-어닐링 처리에 의해 많은 영향을 받는다. 인듐 셀레나이드의 증착방법에는 동시증착법, 브리지만법, 분사 열분해법, 전착법, 졸-겔법, 화학기상증착법, 유기금속화학증착법, 스퍼터링법 등이 있다.

Collection @ chosun

조선대학교 CHOSUN UNIVERSITY

스퍼터링법은 유독성의 셀레늄 함유가스 (H_2Se 또는 Se 가스) 없이 높은 증착률과 좋은 균일성을 제공한다. 동시 스퍼터링법은 간단한 인라인 처리를 수행 할 수eh 있다. CIGS 태양전지에서 기존의 버퍼층을 대체하기 위한 조건들에는 $\leq 10^4 \Omega \cdot cm$ 수준의 비저항, 적절한 밴드갭 에너지(1.68 eV $\leq E_g \leq$ 3.4 eV), 80% 이상의 광투과율 등이 필요하다. 광투과율은 막두께에 직접적인 영향을 받지만, 결함 및 저항 등을 고려해야한다.

셀레늄은 장시간 고온에 노출되면 휘발성이 매우 강한 원소로 알려져 있다. N_2 가스 분위기에서 급속열처리장치 (RTA)의 온도조절을 통한 셀레늄의 휘발성을 이용하여 박막의 화학적 조성비를 조정하는 실험을 진행하였다. RF 마그네트론 스퍼터를 사용하여 $InSe_2$ 단일 타겟으로 기판 위에 증착하였다. 또한 스퍼터링 파워를 조절하여 인듐 셀레나이드 박막의 두께를 조절하였다. 인듐 셀레나이드의 두께는 박막의 구조적, 광학적 및 전기적 특성에 중요한 역할을 한다. 그러나 기존의 연구는 100~800nm 범위에 있었고, CIGS 태양전지에 적용하기 위해 기존의 두께보다 얇은 ≤50 nm 규격의 두께에서 연구를 수행하였다. 실험에서 인듐 셀레나이드 박막의 결정과 구조적인 특성을 분석하기 위해 XRD (X-ray diffraction)를 수행하였고, 전기적, 광학적 특성을 분석하기 위하여 UV-Visible spectrometer와 Hall effect measurement를 사용하였다. 또한 박막의 표면특성을 관찰하기 위해 FE-SEM (field emission scanning electron microscope)을 수행하였다. 급속 열처리 수행한 RF 마그네트론 스퍼터링 방법으로 증착한 인듐 셀레나이드 박막은 동일한 타겟을 사용하여 증착하였음에도 열처리 온도 및 박막 두께에 따라서 상이한 인듐/셀레늄 분율을 나타내었다. 모든 공정조건에서 비정질 특성을 보였으며, 인듐/셀레늄 조성비는 제어 가능하였다. 인듐/셀레늄 조성비 변화를 이용하여 인듐 셀레나이드 박막의 광학적, 전기적 특성을 조절 할 수 있었다. 본 실험을 통해서 $\leq 10^{10} \Omega \cdot cm$의 비저항, ≥87%의 광투과율, 2.875eV $\leq E_g \leq$ 3.048eV의 밴드갭 에너지의 우수한 특성을 가진 인듐 셀레나이드 박막을 개발하였고, 기존 CdS를 대체 가능할 것으로 기대된다.

Collection @ chosun

조선대학교 CHOSUN UNIVERSITY

Ⅰ. Introduction

Copper indium gallium diselenide ($CuIn_{1-x}Ga_xSe_2$, CIGS) thin film solar cells are strongly considered as the most promising thin film solar cells because of its suitable optical absorption (> $10^5 cm^{-1}$), electrothermal stability, high defect-tolerance, no toxic/hazardous pollutants, and a tunable band gap (1.04 eV ≤ E_g ≤ 1.68 eV) by adjusting the chemical composition ratio between Ga and In [1, 2]. CI(G)S thin film solar cells have a conventional structure of glass/molybdenum (Mo)/CI(G)S/buffer layer/transparent conductive oxide (TCO).

Cadmium sulfide (CdS) has been widely applied for the buffer layer in CI(G)S thin film solar cells, which was conventionally fabricated by a wet chemical bath process with very noxious and polluting metal of Cd. To reduce the environmental recycling costs in photovoltaic industries, several Cd-free materials, including zinc selenides and indium selenides [3,4], have been attracted considerable interest in the buffer layer of CI(G)S thin film solar cells. Indium selenides are III-VI compounds with direct band gap, which shows the significant properties for usages in electronics, optoelectronics and photovoltaics [5]. Indium selenides are suitable as a buffer layer in CI(G)S solar cells, because of their porpoerties including in-line preparation by dry process with less toxic materials, stable band gap energy ranging from 1.1 to 3.5 eV, and better heterojunction with CI(G)S absorber layer [3,6-8]. It is usually hard to control the stoichiometry of indium selenides due to the coexistence of non-stoichiometric In_xSe_y, stoichiometric InSe, In_2Se_3, In_4Se_3, In_5Se_7, In_6Se_7, and In_9Se_{11} due to the close formation temperature between each others [6,9-12]. The structural, optical and electrical properties of indium selenides were strongly affected by the preparation method and the post-annealing treatement [11]. Many methods were used to prepare the indium selenides, such as co-evaporation, Bridgeman method, spray pyrolysis, electrodeposition, sol-gel, chemical bath

Collection @ chosun

조선대학교 CHOSUN UNIVERSITY

deposition, metal organic chemical vapor deposition, and sputtering [8,13]. Sputtering method provides high deposition rate and good uniformity without the toxic selenium (Se)-containing gases (H_2Se or Se gas). Co-sputtering method can also perform a simple in-line process after CI(G)S deposition with the same targets for the better heterointerface of the same elemental effusion with the absorber layer.

To replace the indium selenides to the conventional buffer layer in CI(G)S solar cells, there are several requirements to be achieved, such as a resistivity ≤ 10^4Ω·cm, a proper band gap energy (1.68 eV ≤ E_g ≤ 3.4 eV), and an optical transmittance ≥ 80% [14-16]. The optical transmittance is directly influenced by the film thickness, but the defects and resistivity should be considered at the same time [17,18]. Se is also known as a very volatile element in heat treatment at high temperature for long duration [19-21].

In chapter3, rapid thermal annealing (RTA) was performed in N_2 gas ambient to adjust the chemical composition ratio in the indium selenide thin films by controlling the Se-volatilization from the precursors with a short process time and reduced thermal exposure [22]. In chapter4, the thickness of Indium selenide thin film was controlled by adjusting the sputtering power. The thickness of indium selenides played an important role in the structural, optical and electrical properties of them, however the variations of film thickness in the previous study was in the range from 100 to 800 nm which was higher scale than the conventional thickness (~ 50 nm) applied to CI(G)S thin film solar cells [17,23-25].

In this thesis, indium selenides were fabricated by sputtering method without any toxic gas and annealed by RTA in N_2 gas ambient, which is dealt with an experimental examination of the influences of the nano-scaled (≤ 70 nm) film thickness on the structural, optical and electrical properties of indium selenides.

Collection @ chosun

조선대학교
CHOSUN UNIVERSITY

Ⅱ. Theoretical Background

A. CIGS Thin Film Solar Cells

1. Structure of CIGS Thin Film

Structure of CIGS solar cell is made by the formation of a multi-layer film, such as Fig 1. Mo and ZnO is used in the back and front electrode of the thin film, while CIGS thin film is used as the absorber layer. Indium selenide was located as a buffer layer between the absorber layer and ZnO thin film as a front-electrode/window layer. General structure of CIGS thin film solar cell is shown in as follow.

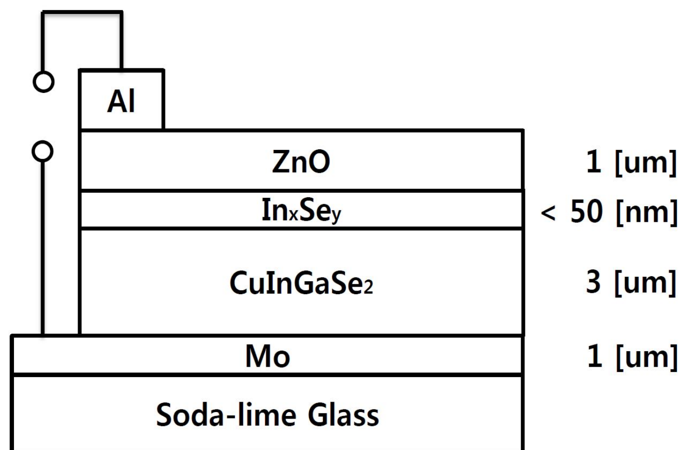

Fig. 1 Structure of CIGS solar cells used as a buffer layer to indium selenide

Collection @ chosun

조선대학교 CHOSUN UNIVERSITY

a. Substrate

Soda lime glass (SLG) has been used as the general CIGS solar cell substrate material because it has a number of advantages for high-efficiency and inexpensive solar cells. SLG has the additional effect in the cell with the spread of Na into CIGS absorber because the incorporated Na improves open-circuit voltage (V) and fill factor (FF) [26,27]. In addition, the use of SLG substrate reduces the solar cell production cost and provides smooth surface for multi-layered structure.

b. Back contact

Recently, molybdenum (Mo) is used for a back contact with CIGS absorber. The Mo film is typically deposited on a substrate using a DC sputtering. Mo with a thickness of approximately 1 ㎛, generally deposited by DC sputtering, is used for back contact in CIGS solar cells. Mo has low contact resistance to the CIGS. It is common to control the properties of Mo by varying the deposition pressure.

c. Buffer layer

Hetero-junction solar cells have a large lattice mismatch at the interface between absorber and window layers. Introduction of the buffer layer in particular In_xSe_y, between CIGS absorber and window layers can improve the bonding property due to the better hetero-interface with the same elemental effusion to the CIGS absorber layer.

d. Window layer

ZnO thin film as a window layer is typically deposited by RF sputtering method. CIGS and ZnO thin film the p-n junction can achieve, but the interfacial defects can occur because of the large lattice mismatch [28,29]. ZnO thin film has band gap energy of about 3.4 eV and light transmittance of 80%.

Collection @ chosun

조선대학교
CHOSUN UNIVERSITY

e. Grid

In order to prevent the resistance loss due to the formation of Al_2O_3 between the grid and ZnO [30], the insertion of a thin Ni layer is common: bilayer Ni/Al grid structure. Grids of the Ni/Al was deposited on the surface of the ZnO using the e-beam evaporator.

2. Characterization of Thin Films

Scattering, reflection, fluorescence/phosphorescence (absorption and re-emission), photochemical reaction (absorbance and bond breaking), and absorbance can occur while radiation interacts with matter. Generally, optical transmission are computed by measuring the transmittance from UV-visible spectroscopy.

When light passes through or is reflected from a specimen, the absorbed amount of light is the distinction between the incident radiation (I_0) and the transmitted radiation (I). The absorption of light is presented as either transmittance or absorbance. In general, Optical transmittance is expressed in terms of a fraction of the 1 or as a percentage. It is defined using the Beer-Bouguer-Lambert Law as follows:

$$T = I/I_0 \quad or \quad \%T = (I/I_0) \times 100 \tag{2-1}$$

Absorbance of the thin films was calculated at a particular wavelength of light using the equation,

$$A = -\log T = \log(I_0/I) \tag{2-2}$$

, where A is the absorbance, T is the transmittance, I is the incident radiation intensity, and I is the transmitted radiation intensity. Absorption coefficient (α) which was calculated using the Beer-Lambert law in the

Collection @ chosun

조선대학교
CHOSUN UNIVERSITY

high-absorption region [31,32]:

$$\alpha(v) = (2.303/d)A \tag{2-3}$$

, where d and A are the thickness and absorbance of film, respectively. This is a measure of how far an incident photon with a given wavelength can be absorbed below the surface of a thin film to a depth at which the irradiance decreases to 37% (*i.e.*, *1 / e*) of its incident level [33,34]. The penetration depth (Γ) can be represented using the reciprocal of the absorption coefficient ($\alpha = 1/\Gamma$).

Band gap (E_g) for direct band gap materials can be obtained by an extrapolation in the linear region of each curve to the energy axis from $(\alpha h\upsilon)^2$ versus the photon energy ($h\upsilon$) in the Tauc plot. The band gap energy is found where the suited line pass through the energy-axis. The band gap (E_g) of CIS thin films were also computed using the formula

$$E_g = hv/\lambda \tag{2-4}$$

, where h is Planck's constant (4.135667×10^{-15} eVs), λ is an absorption onset wavelength (nm) (1 / e = 37%) and c is the velocity of light (3×10^8 m/s).

The mobility, the free carrier density and the resistivity in a semiconductor are obtained using the Hall effect measurement. Also whether the specimen is of p-type or n-type conductivity can be distinguished. The source of the Hall effect is the force that acts on electrons that move vertical to a magnetic field. This force sets up the so called Hall voltage (V_H) in the direction vertical to the current and the magnetic field. This voltage is contained in the definition of the Hall coefficient (R_H).

$$R_H = tV_H/BI \tag{2-5}$$

Collection @ chosun

조선대학교 CHOSUN UNIVERSITY

In Equation (2-5), the supposition is that the magnetic field is vertical to the film surface. The sign of R_H will be dissimilar reliance on if the conduction in the films is owing to holes or electrons. Therefore, the density of carrier is given by the following equations.

$$p = 1/qR_H \text{ or } n = -1/qR_H \quad (2\text{-}6)$$

If both carrier types influence to the conduction the condition is more complicated. For simplicity energy-independent carrier scattering mechanisms is supposed when deduce Equation (2-6). This simplification is commonly used when evaluating thin films. The majority carrier mobility is calculated from the following equation.

$$\mu = |R_H|/\rho \quad (2\text{-}7)$$

The carrier density and mobility of the thin films will be evaluated by the Van der Pauw method. In this technique the film should be uniform in thickness and not include any isolated holes. The contacts should be ohmic, sufficiently small and located at the circumference of the specimen. A number of resistance measurements in the Van der Pauw-method are made. The current is driven between two contacts for each measurement while the voltage simultaneously is measured at the two other contacts. Resistivity measurements are realized between neighbouring contacts without magnetic field. Carrier density and mobility are calculated from measured values between opposite contacts with magnetic field contained.

Collection @ chosun

조선대학교
CHOSUN UNIVERSITY

B. Principles of Sputtering

Vacuum deposition and sputtering is used as the physical thin film deposition method. The vacuum deposition method has been widely used for a long time with a simple structure. This method has some drawbacks which is difficult to apply for a large area with an internal contamination to obtain the good quality in the chamber. The sputtering method is also widely used to deposit various metals and insulators. In particular, the sputtering method uses a mixture of different gases in the inert gas, so it is useful for preparing the oxide and nitride thin films.

The basic principle of the sputtering method is that the atoms, ejected from the target surface of the target material by the bombardment of the energetic particles, are build up on the surface of the substrate. Sputtering yield (S) is one the most important parameters in sputtering process, which was defined as the mean number of the atoms removed from the target to the incident particles as follow:

$$S = N_r \ / \ N_i \qquad (2\text{-}8)$$

, where N_r is number of the removed atoms and N_i is number of the incident ions. While the inert gas flows in the chamber of the vacuum, the direct current power of 1 W/cm^2 is applied on the target and then the plasma is generated between the substrate and the target. The inert gas is ionized by a high-power electric fields of a cation ion are accelerated by the cathode by a direct current electric field will hit the target surface.

1. RF Sputtering

RF sputtering has been developed in order to deposit a thin film of the insulators while DC sputtering cannot be used for sputtering of insulators.

Collection @ chosun

조선대학교 CHOSUN UNIVERSITY

Particularly, standard RF frequency of 13.56 MHz is widely used in the range of 5~30 MHz, which is the reason why the frequency was internationally accepted in the plasma process. Alternating voltage with a high frequency can neutralize the positive-charged surface with electrons from the plasma to continue the sputtering of insulators. RF sputtering can also deposit the conducting materials at higher rate.

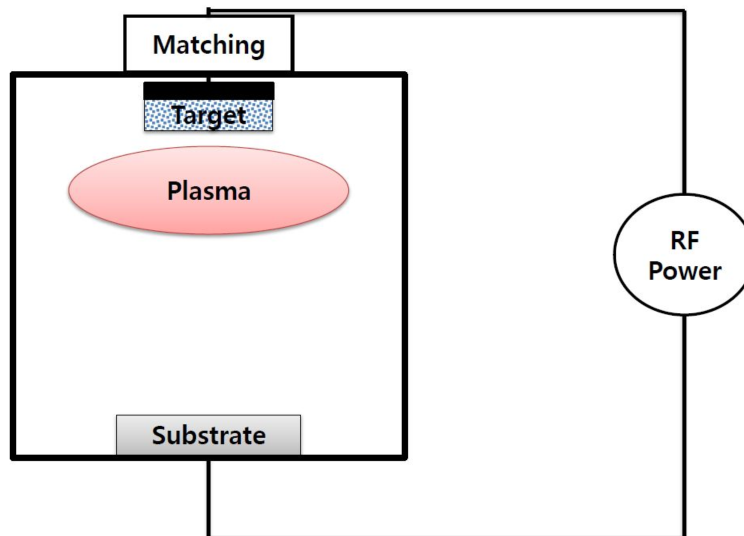

Fig. 2 RF sputtering configuration

2. Magnetron Sputtering

Magnetron sputtering is similar to the RF sputtering, however, the cathode is equipped with a permanent magnet applying a magnetic field which makes the direction parallel to the target surface. These permanent magnets are attached by a target called by a magnetron target. When the magnetic field is parallel to the target surface, the electric field is perpendicular. The former are a turning movement towards the force of Lorentz, it is accelerated to a

Collection @ chosun

조선대학교 CHOSUN UNIVERSITY

spiral motion. This prevents electrons from leaving the plasma near the target and continues to turn because it is held very close to the peripheral surface of the target, so that the plasma density of the region near the ionization rate increases. It may cause a lot of ion discharge currents and then the sputtering rate to be increased. Therefore, the electrons, decreasing in the collision of the substrate, improve the deposition rate and then the low pressure sputter can also be possible. The deposition rate of the thin film can be improved to about 50 times and deposition pressure can be lowered even to 1 mTorr. A typical intensity of the magnetic field is 200-500 G. In addition, the heating in sputtering from the chamber walls and the substrate decreases during deposition. Drawbacks of the magnetron target are that the target is not consumed uniformly. In other words, magnetic lines of force in the area close to a straight line more sputtering occur. Therefore, a uniform deposition rate of the target can not be obtained. Many different types of targets have been developed in order to improve the utilization of the target as well as non-uniformity of deposition.

Fig. 3 RF magnetron sputtering equipment (I.D.T. ENG)

Collection @ chosun

조선대학교
CHOSUN UNIVERSITY

C. Principles of Annealing : Rapid Thermal Annealing (RTA)

Rapid thermal anneal (RTA) is a subset of rapid thermal processing. RTA equipment rapidly raises the surface temperature of the sample using the halogen lamps. The reflector is coated with gold (Au) to increase in the reflectivity. By giving an inert gas flow with the mass flow controller (MFC), the amount of gas was adjusted in the RTA. RTA is generally used for annealing after the coating of the electrode material for the electrical characterization of semiconductor material. Changing the heat treatment conditions of the amorphous silicon is used to observe the crystal changes in to the zoom. There are advantages of RTA can be quickly heated or cooled to the temperature can significantly reduce the thermal budget. The RTA did not receive much in the limelight. The reason is that uniformly maintains the temperature of the whole wafer, each time a replacement for other wafer such as the wafer temperature-maintaining time characteristic, the temperature of the wafer it is difficult to accurately measure and control. However, recent advances in this technical problems of the number of the temperature measurement and temperature control techniques are significantly improved. The various heat treatment process of the furnace is going to be replaced by the RTA. Especially, RTA is easy to control a single wafer processing apparatus and the number of variables in the working environment.

Fig. 4 Rapid thermal annealing equipment (GD Tech)

Collection @ chosun

조선대학교 CHOSUN UNIVERSITY

D. Analysis of Thin Film

1. Field Emission Scanning Electron Microscope (FESEM)

FESEM stands for field emission scanning electron microscope. FESEM is microscope used to electrons (particles with a negative charge) instead of light. These electrons are released by field emission sources. The object is retrieved by electrons according to a zig-zag pattern. FESEM is used to visualize very small topographic information on the surface or fractioned objects or entire.

Physics, chemistry, biology researchers can apply this technique to observe the structure of less than 1 nm (= billion of a millimeter). Electrons are emitted from the field emitter source and accelerated by a high electric field gradient. Within the high vacuum column are focused and deflected by electronic lenses to produce a narrow scan beam. This is bombarded with the object. That the resulting secondary electrons emitted at each point of the object. Angle and speed of these secondary electrons to the surface structure of the object. The detector detects secondary electrons and generates an electronic signal. This signal is amplified and converted into a video scanned image that can be seen on a monitor and to a digital image that can be storage and processing.

2. X-Ray Diffraction (XRD)

Spacing between the atoms of any crystal is d, and the atoms are arranged on the parallel lattice planes (a, b, c in order). The X-ray of wavelength λ in the crystal is irradiated by the incident angle θ. Then, the X-rays are scattered in all directions by the atom. And X-rays are strengthened by the interference effect. This phenomenon is called the diffraction phenomenon, and X-ray generated diffraction phenomenon is

Collection @ chosun

조선대학교
CHOSUN UNIVERSITY

called by X-ray diffraction. If the diffraction phenomenon caused between the incident X-ray wavelength λ and incident angle θ and the lattice plane spacing d, the following relationship is established.

$$2dsin\phi = n\lambda \tag{2-9}$$

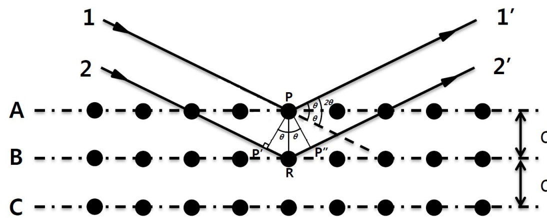

Fig. 5 Principles of X-ray diffraction (XRD) analysis

The above equations is called the Bragg equation. If the incident angle θ of X-rays is determined, the lattice plane spacing d becomes determined. Usually, X-ray diffraction is used 2θ (diffraction angle) than incident angle θ. The reason for this is well reflected on the geometric arrangement of the measuring system. When recording the diffraction X-ray intensity, the intensity can be obtained form a plurality of different diffraction peaks. The crystal structure is different to the material, and diffraction type (pattern) is a unique value for the material.

Fig. 6 XRD equipment (Philips X'pert-PRO-MRD XRD)

Collection @ chosun

조선대학교 CHOSUN UNIVERSITY

3. Hall Effect Measurement System

Hall effect is due to the current characteristics of the conductor. The current is generally comprised of electrons, hole, and ion. If the magnetic field is present that is not parallel to movement direction of the moving charge, these electrons is forced, called the Lorentz force. When such a magnetic field is absent, the charges follow almost straight, 'line of sight' paths between collide with phonons, impurities, etc. However, if the magnetic field of the vertical component is applied, their paths to colliding are curved. So the moving charge is accumulated in the corner of the material. This leaves opposite and equal charges exposed on the other face, where there is a scarcity of moving charges. As a result, an asymmetric distribution of charge density of the Hall element, that is vertical to both the 'line of sight' paths and the magnetic field applied. The separation of charging establishes an electric field that stems the movement towards further charge, so a steady electrical potential is established during the charge is flowing. In the classical point of view, there are electrons moving in the same average direction in the case of the hole or electron conductivity. This cannot explain the opposite sign of the observed Hall effect. The difference is that electrons in the maximum of the valence band have opposite group wave vector direction and velocity when moving, which can be economically treated as if positively charged particles moved in the opposite direction to the electrons. As show in Figure 7, a current flows in the semiconductor or the metal foil having a thickness d, the magnetic field is passed vertically. Direction of the magnetic field is the z-direction (coming from the ground), the current-flow direction is the x-direction, direction of the Hall electromotive force is the y-direction.

The electric field (y-direction) is generated because the charges building up on the inside of the sample. At this time, the power to the electric field acting on a charge is as follow:

Collection @ chosun

조선대학교
CHOSUN UNIVERSITY

$$F_y = qE_y \tag{2-10}$$

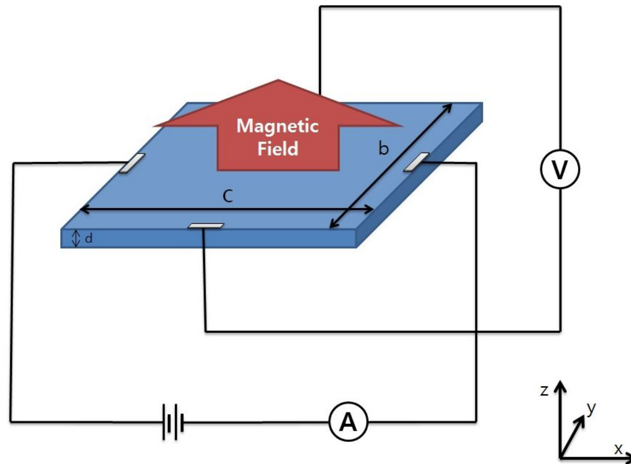

Fig. 7 Schematic diagram of the Hall-effect measurement

Force acting on the sample inside the charge moving at a speed *v* in the x-axis direction is as follow:

$$F_y = -qvB \tag{2-11}$$

In the above equations, two forces are achieve balance. This comes the expression as follow:

$$qE_y = qvB \tag{2-12}$$

Where the thickness of the sample is *d*, *b* is the width, and *c* is the length, current *I* is expressed as follow:

$$I = nqvdb \tag{2-13}$$

Since the voltage across the voltmeter is $V = E_y b$, the measured *I*, *B*, *V* can be obtained in the *n*. Also $V = vBb$ and substituting implanted in (2-13), *v* erased to ask the *n* follow:

Collection @ chosun

조선대학교
CHOSUN UNIVERSITY

$$n = \frac{IB}{qdV} \tag{2-14}$$

So n must be a positive value, this can be determined from the sign of q and V which is the voltage applied to the lower surface on the basis of the upper surface of the sample. Hall coefficient can be obtained from equation (2-14).

$$R_H = \frac{dV}{IB} = \frac{1}{nq} \tag{2-15}$$

R_H is used to determine the type of charge carriers. On the other hand, if measuring the voltage drop V_x of the Hall element can calculate the specific resistance.

$$\rho = \frac{V_x db}{Ic} \tag{2-16}$$

Since resistivity (ρ) is the reciprocal of the electric conductivity (σ) of the charge carriers, Mobility (μ) of the charge carriers is expressed as follow:

$$\mu = R_H \sigma \tag{2-17}$$

Fig. 8 Hall effect measurement system equipment
(Accent Optical Technologies. HL5500PC)

Collection @ chosun

조선대학교
CHOSUN UNIVERSITY

4. UV-Visible Spectrophotometer

Principle of a typical spectrometer are shown in Fig. 9. Features of this instrument is relatively simple. A light beam from a visible and/or ultraviolet (UV) light source (colored red) is separated from a prism or diffraction grating into its component wavelengths. Each single color beam is then split into two equal intensity beams by the half-mirror device. One beam, the sample beam (colored red), is passed through a small transparent container containing a solution being studied in a transparent solvent. Other beam, the reference (colored blue), is passed through the same cuvette containing a solvent. The strength of the electron beam is measured by a detector and compared.

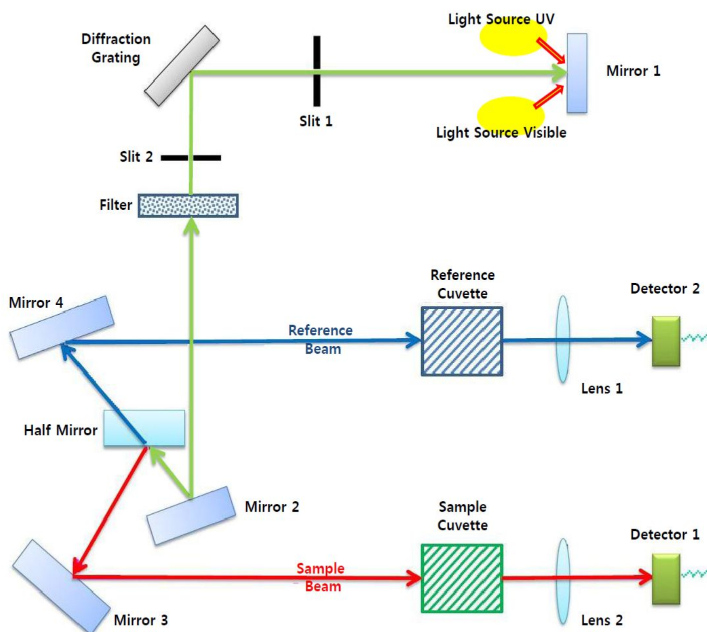

Fig. 9 Diagram of UV-visible spectroscopy

Collection @ chosun

조선대학교 CHOSUN UNIVERSITY

The intensity of the reference light, which suffers little or no light absorption, is defined as I_0. I is defined as the intensity of the sample beam. For a short time, as described automatic analyzer scans all the wavelength components. Scanned UV region the sample compound does not absorb light of a predetermined wavelength, $I=I_0$. However, if the sample compound absorbs light, I is less than I_0. These differences can be represented as a graph versus wavelength.

Absorption may be represented by a transmittance ($T=I/I_0$) or absorbance ($A=\log(I_0/I)$). If no further absorption occurred, T = 1 and A = 0. Most of the analysis absorbance is shown on the vertical axis, And general observation range is from 0 (100% transmittance) to 2 (1% transmittance). Wavelength at the maximum absorbance is a characteristic value, expressed as λ_{max}.

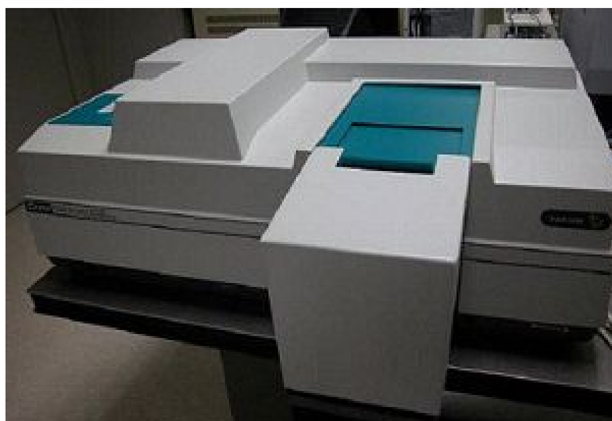

Fig. 10 UV-visible spectrophotometer equipment
(Varian Techtron. Cary 500 scan)

Collection @ chosun

조선대학교 CHOSUN UNIVERSITY

III. Non-stoichiometric Amorphous Indium Selenide Thin Films

A. Experimental Details

Corning glass substrates of 20×20 mm was used to deposit the approximately 50-nm-thick thin films by RF magnetron sputtering (IDT Engineering Co.). Commercial target of $InSe_2$ (LTS Chemical Inc., 99.99% purity, 2inches-diameter) were used with a fixed set of process parameters : a pre-sputtering for 3minutes, Ar gas flux of 50 sccm, base pressure of 1.0×10^{-6} Torr, substrate to distance of 5.0 cm, RF sputtering power of 20 W, and vacuum pressure of 7.5×10^{-3} Torr during the sputtering process for 9 minutes at room temperature. RTA (GD-TECH Co., GRT-100) treatment of the 50-nm-thick thin films was performed to improve the temperature uniformity over conventional furnace for 1 minute in N_2 gas ambient by a variation of temperatures from 400°C to 700°C with an interval of 100°C [19,20].

The microstructure of the thin films was analyzed by X-ray diffraction (XRD, Philips, X'pert-PRO-MRD, CuKα= 0.15405 nm, 40 kV, 30 mA) and Field emission scanning electron microscope (FESEM, JEOL, JSM-7500F). The XRD patterns were obtained over the range of 10–90°2θ. Energy-dispersive X-ray (EDX, Oxford Instruments, INCA) installed in the FESEM apparatus was used to characterize the chemical composition ratio of Se in the as-deposited and RTA-treated thin films. The optical properties of the as-deposited and RTA-treated thin films were measured using an ultraviolet-visible spectrophotometer (Varian Techtron, Cary500scan) in the range of 400–1500 nm. The electrical properties of the thin films, including the resistivity, carrier concentration and the mobility, were characterized using a Hall Effect measurement system (Accent Optical Technologies, HL5500PC) at room

Collection @ chosun

조선대학교 CHOSUN UNIVERSITY

temperature.

Table 1. The sputtering and annealing process condition

<table>
<tr><td rowspan="6">Sputtering</td><td rowspan="3">$InSe_2$ Target</td><td>RF Power</td><td>20 W</td></tr>
<tr><td>Sputtering Time</td><td>270 sec</td></tr>
<tr><td>Film Thickness</td><td>50 nm</td></tr>
<tr><td colspan="2">Vacuum Pressure</td><td>7.5×10^{-3} Torr</td></tr>
<tr><td colspan="2">Ar</td><td>50 sccm</td></tr>
<tr><td colspan="2">Pre-sputtering Time</td><td>3 min</td></tr>
<tr><td rowspan="5">Annealing</td><td colspan="2" rowspan="5">RTA
Temperature (Time)</td><td>As-dep</td></tr>
<tr><td>400℃
(60 sec, Included rising time)</td></tr>
<tr><td>500℃
(60 sec, Included rising time)</td></tr>
<tr><td>600℃
(60 sec, Included rising time)</td></tr>
<tr><td>700℃
(60 sec, Included rising time)</td></tr>
</table>

B. Results and Discussion

Figure 11 shows the microstructure of indium selenide thin films with SEM images and XRD spectra of the (a) as-deposited and RTA-treated specimens by changing annealing temperatures of (b) 400°C, (c) 500°C, (d) 600°C, and (e) 700°C. The diffraction spectra were examined by scanning 2θ in the range of 10–90°. The prominent peak in spectra except the broad and weak peaks was not detected in both the as-deposited and RTA-treated indium selenide thin films at the temperatures ≤ 700°C, which means that the

Collection @ chosun

조선대학교 CHOSUN UNIVERSITY

microstructure remained amorphous nature. This result agrees with previous studies [35–37]; however, there is a subtle difference. Bernède *et al* have reported on the crystallization of indium selenides during annealing above critical temperature (T_{crit}, approximately ~320°C), which is a temperature showing an irreversible increase in conductivity, was caused by the formation of In_2Se_3 microcrystallites [37]. Lu *et al.* have reported more accurately that the indium selenides of In_2Se, InSe, and In_2Se_3 were formed sequentially at the temperature above 105°C, 205°C, and 320°C, respectively [38]. In this experimental observation, the thin films were insufficient to be crystallized although RTA was performed above 400°C > T_{crit}. Crystallinity can't seem to be the most important factor in the properties of indium selenides after all. SEM images in Fig. 11 show the surface morphology of indium selenide thin films for both as-deposited and thermal treated samples. All samples show good coverage of indium selenides in spite of their thickness ~50 nm on glass substrate without pinhole. Well defined grain was not observed, which agrees the XRD results showing the amorphous in both the as-deposited and RTA-treated indium selenide thin films regardless of the annealing temperature. Some nanospheres, which were the solidified In precipitates similarly in the previous literatures [35, 36], were shown in the as-deposited and RTA-treated samples at the temperatures ≤ 600°C. As increasing the annealing temperature, the nano spheres decreased and disappeared with marks on the surface at 700°C.

Chemical compositions of indium selenide thin films for both as-deposited and thermal treated samples were examined from EDX, as shown in Fig. 12. The as-deposited sample has a 47.87 at% and 52.13

Collection @ chosun

조선대학교 CHOSUN UNIVERSITY

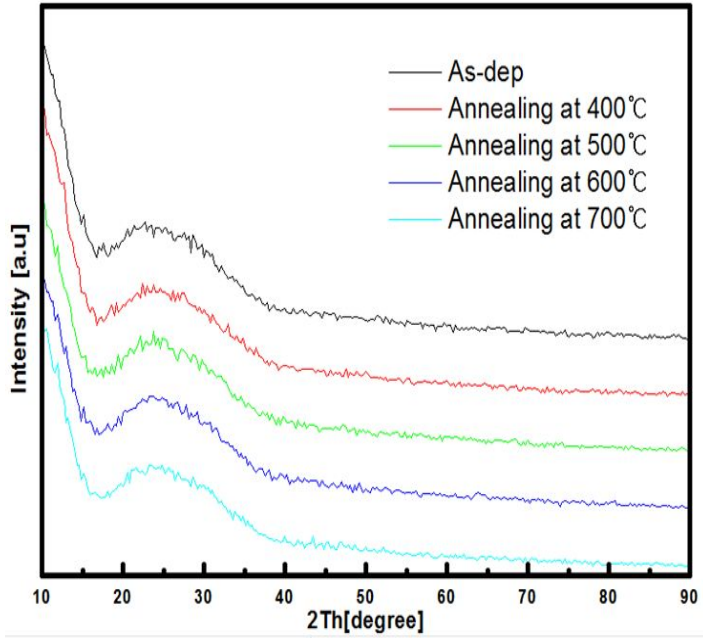

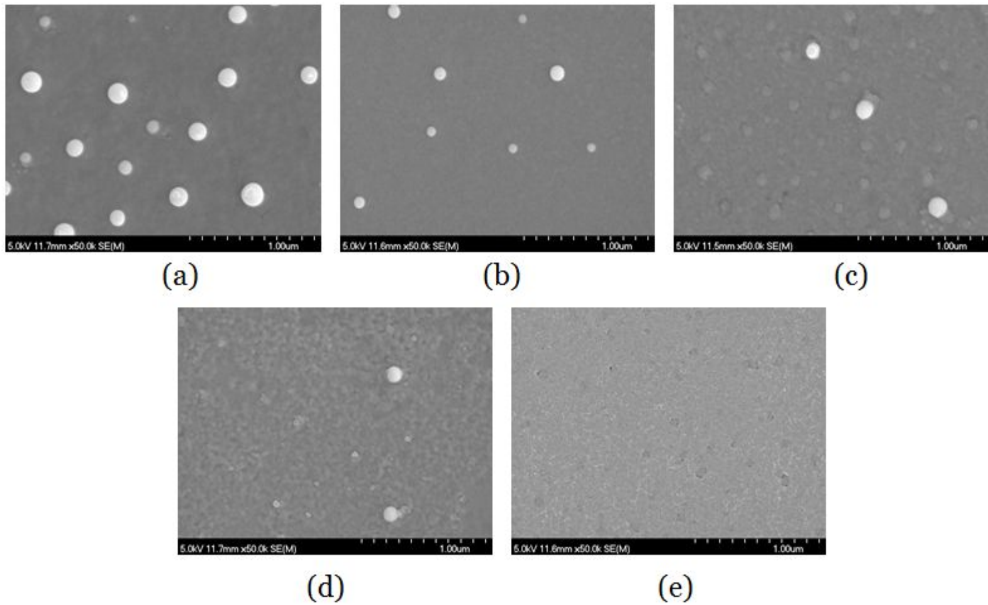

Fig. 11 FESEM images and XRD spectra of the (a) as-deposited and the RTA-treated indium selenide thin films at the annealing temperatures of (b) 400℃, (c) 500℃, (d) 600℃, and (e) 700℃

Collection @ chosun

조선대학교
CHOSUN UNIVERSITY

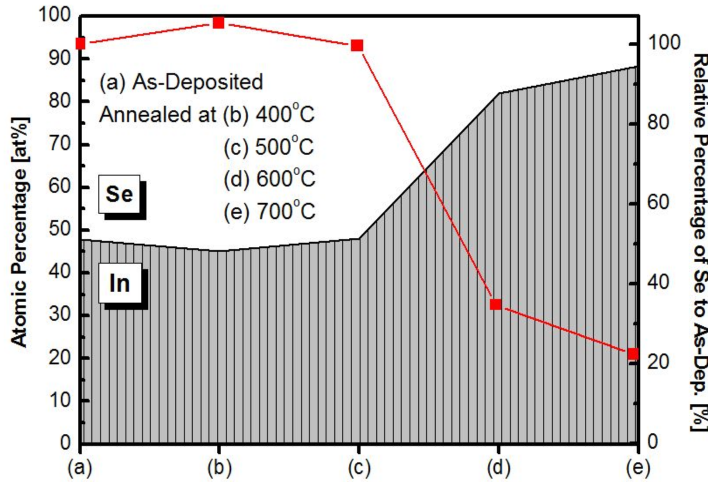

Fig. 12 EDX result for specimens of the (a) as-deposited and the RTA-treated indium selenide thin films at the annealing temperatures of (b) 400℃, (c) 500℃, (d) 600℃, and (e) 700℃

at% of In and Se in the film, respectively. Once thermal treated, the chemical composition remained similar until the temperature of 500°C. Above 600°C, the volatilization of Se occurred and the chemical composition of Se decreased to fewer than 18.10 at%.

This is 34.73% level to Se in the as-deposited sample. The calculated molar ratios of Se to In were 1.769, 1.571, 0.323, and 0.192 in RTA-treated indium selenide thin films at 400°C, 500°C, 600°C, and 700°C, respectively. These molar ratios don't correspond with the reported stoichiometries, such as InSe, In_2Se_3, In_4Se_3, In_5Se_7, In_6Se_7, and In_9Se_{11}. The molar ratios were non-stoichiometries approaching the stoichiometric compositions of In_4Se_7, In_2Se_3, In_3Se and In_5Se in the amorphous indium selenide thin films, respectively.

Amorphous indium selenides are known to exhibit anomalous properties compared to other chalcogenides [36], an influences of the change in chemical composition should be investigated on optical and electrical properties of these amorphous indium selenides. Figure 13 shows the

Collection @ chosun

조선대학교 CHOSUN UNIVERSITY

experimentally-measured optical transmittance in the visible to near-infrared (NIR) spectral region of the RTA-treated indium selenide thin films. Mean optical transmittance of indium selenide thin films with the thickness of ~50 nm was ≥ 63% in the visible to NIR spectral region (400–1600 nm). Mean optical transmittance improved from 63.99% to 75.33% as increasing annealing temperature from 400°C to 700°C in RTA treatment. An increased chemical composition of In, which can reformulate a decreased chemical composition of Se by increasing the annealing temperature, in amorphous nature showed the similar tendency to increase in the optical transmittance.

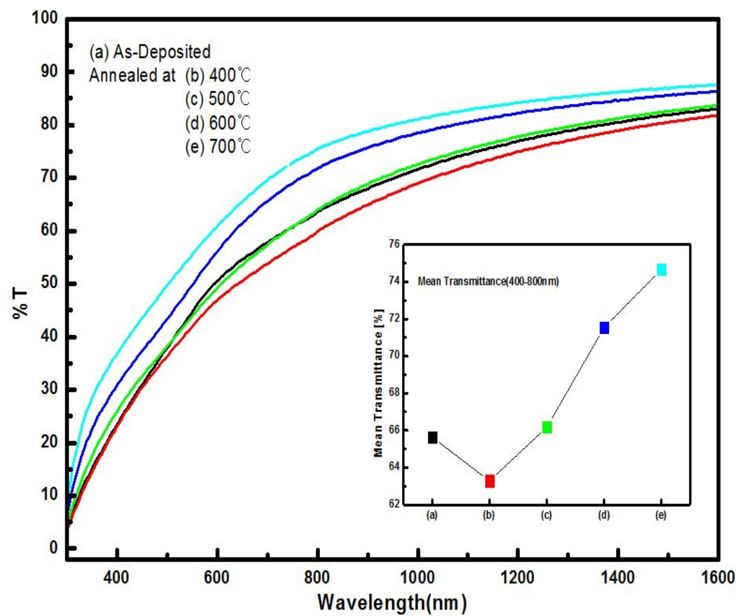

Fig. 13 Optical transmittance for specimens of the (a) as-deposited and the RTA-treated indium selenide thin films at the annealing temperatures of (b) 400℃, (c) 500℃, (d) 600℃, and (e) 700℃

Collection @ chosun

조선대학교 CHOSUN UNIVERSITY

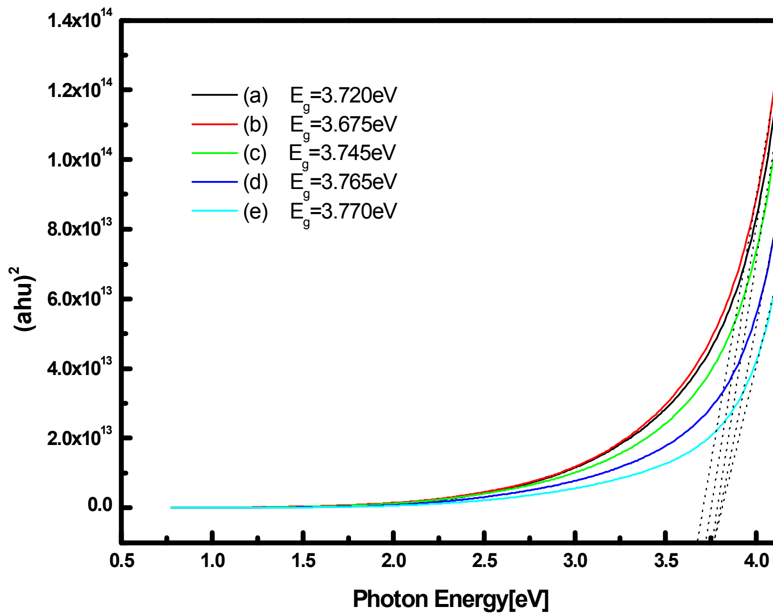

Fig. 14 Band gap energy of the (a) as-deposited and the RTA-treated indium selenide thin films at the annealing temperatures of (b) 400℃, (c) 500℃, (d) 600℃, and (e) 700℃

Hall Effect measurements were performed to investigate some electrical properties of the RTA-treated indium selenide thin films, including the conductivity type, carrier mobility, resistivity and carrier concentration, by varying the annealing temperature, as shown in Fig. 15. Carrier concentration of the RTA-treated indium selenide thin films, showing p-type conductivity, increased logarithmically in the order-of-magnitude range from 10^{11} to 10^{14} cm^{-3} of excessive holes at the annealing temperatures ≤ 600°C. The carrier concentration was abruptly changed after RTA treatment at the annealing temperature of 700°C (*i.e.*, at the high chemical composition of In), which showed $10^{17} cm^{-3}$-ordered n-type conductivity of excessive electrons in the specimen. Similar results could be observed in the prior studies revealing the conductivity of indium selenides became n-type from p-type for high In

Collection @ chosun

조선대학교 CHOSUN UNIVERSITY

concentration. There was a difference in this study remained amorphous nature (Fig.10), which was caused by increase in number of crystallites (atomic arrangements) including In_2Se_3, InSe and In_4Se_3 with n-type conductivity with an increase in indium concentration in the indium selenides. The increased carrier concentration in p-type amorphous indium selenides at the temperature ≤ 600°C was attributed to the excess of indium atoms as well as the reduction in the donor center of V_{Se} and/or increase in the acceptor centers of V_{In} and Se_i. The main attribution to the change in the carrier conductivity type at the temperature of 700°C was thought to be due to the decrease in V_{In} with more increase in indium concentration in the indium selenides. Carrier mobility decreased with increasing the annealing temperature.

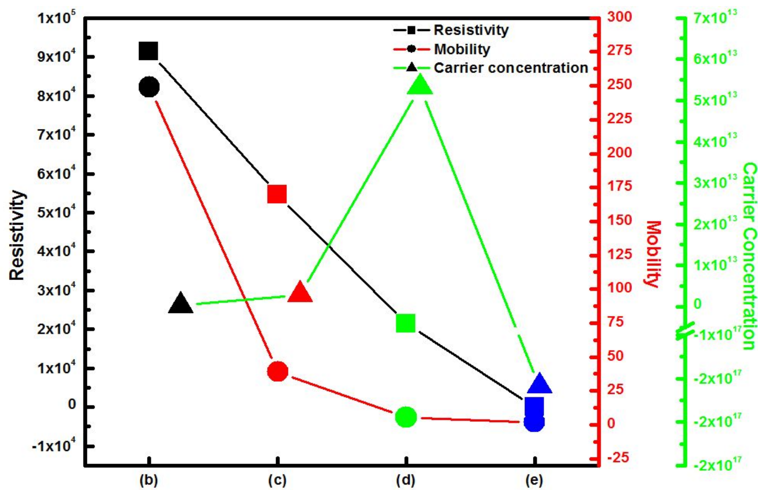

Fig. 15 Resistivity, carrier concentration and carrier mobility of the (a) as-deposited and the RTA-treated indium selenide thin films at the annealing temperatures of (b) 400℃, (c) 500℃, (d) 600℃, and (e) 700℃

As increasing In concentration, the dissolved In in the Se chains tends to bind Se to increase the length of amorphous short-range order then the

Collection @ chosun

조선대학교 CHOSUN UNIVERSITY

mobility decreased. Resistivity of the RTA-treated indium selenides was in the range of 10^1–10^5Ω·cm. This is smaller than the reported values (10^3–10^{11} Ω·cm) of CdS thin films as the conventional buffer layer for CIGS thin film solar cells. The resistivity generally depends of the carrier concentration and carrier mobility. The main attribution to the decrease in the resistivity at the temperature of 700°C was caused by the rapidly increase in carrier concentration of the excessive electrons with n-type conductivity in the specimen.

Collection @ chosun

조선대학교 CHOSUN UNIVERSITY

IV. Nano-scaled Thickness of Indium Selenide Thin Films as a Buffer Layer

A. Experimental Details

Indium selenide thin films were prepared on Corning glass substrates of 20×20 mm. RF magnetron sputtering (IDT Engineering Co.) method was used with a commercial target of InSe2 (LTS Chemical Inc., 99.99% purity, 2 inches-diameter) were used. A set of process parameters was fixed: a pre-sputtering for 3 minutes, Ar gas flux of 50 sccm, base pressure of 1.0×10^{-6} Torr, substrate to distance of 5.0 cm, RF sputtering power of 15 W, and vacuum pressure of 7.5×10^{-3}Torr at room temperature. Film thickness was varied 30, 40, 50, 60, 70 nm by control of sputtering time with the deposition rate of 5.66 nm/min. RTA (GD-TECH Co., GRT-100) treatment of the different-thickness indium selenide precursors was performed at 700°C for 1 minute in N_2 gas ambient with a ramp-up speed of 7.78°C/sec. RTA was performed to adjust the chemical composition ratio in the indium selenide thin films by controlling the Se-volatilization from the precursors with a short process time and reduced thermal exposure [21,22].

The structural property of the indium selenide thin films was analyzed by X-ray diffraction (XRD, Philips, X'pert-PRO-MRD, Cu Kα = 0.15405 nm, 40 kV, 30 mA) over the scan range of 2θ = 10-90°. An energy-dispersive X-ray spectroscopy (EDX, Oxford Instruments, INCA) attached on a field emission scanning electron microscope (FESEM, JEOL, JSM-7500F) was used to characterize the chemical composition ratio of each element in the RTA-treated indium selenide thin films. The optical properties of the different-thickness indium selenide thin films were measured using an ultraviolet-visible spectrophotometer (Varian Techtron, Cary500scan) in the range of 300-1800 nm. The electrical properties of the indium selenide thin

Collection @ chosun

조선대학교 CHOSUN UNIVERSITY

films, including the carrier concentration, resistivity and the mobility, were characterized using a Hall Effect measurement system (Accent Optical Technologies, HL5500PC) at room temperature.

Table 2. Sputtering conditions for the adjustment of the film thickness

Sputtering	$InSe_2$ Target	RF Power	20 W
		Sputtering Time	5.3 min
			7.06 min
			8.83 min
			10.5 min
			12.3 min
	Vacuum Pressure		7.5x10^{-3} Torr
	Ar		50 sccm
	Pre-sputtering Time		3 min
RTA	Temperature (Time)		700℃ (60 sec, Without rising time.)

B. RESULTS AND DISCUSSION

Figure 16 shows the XRD patterns of the RTA-treated indium selenide thin films by changing film thickness of (a) 30, (b) 40, (c) 50, (d) 60, and (e) 70 nm. The diffraction spectra, examined by scanning 2θ in the range of 10–90°, indicate that the prominent peak in spectra except the weak peaks was not detected in all specimens regardless of the film thickness. This means that the microstructure was in amorphous nature [17,35,36]. The preliminary studies on the annealing temperature and duration in RTA process did not show a great difference in XRD spectra of indium selenide thin films [39]. In this experimental demonstration, the indium selenide thin films were insufficient to be crystallized although RTA was performed around 700°C,

Collection @ chosun

조선대학교 CHOSUN UNIVERSITY

although the crystallization of indium selenides has been reported that In_2Se, InSe, and In_2Se_3 were formed sequentially at the temperature above 105°C, 205°C, and 320°C, respectively [38].

SEM images in Fig. 17 show the surface morphology of indium selenide thin films with different thickness. Unform and dense coverage of indium selenides without pinhole was shown in all samples despite their thickness ≤ 70 nm on glass substrate. Well defined grain was not observed because the RTA-treated atoms have insufficient mobility for the crystallization of indium selenides [40], which agrees the XRD results showing the amorphous in all indium selenide thin films regardless of the film thickness. Slightly classifiable grains around 20–30 nm were seen in (a) 30 and (c) 50 nm whereas there is no constant trend in grain to the film thickness.

Chemical compositions of indium selenide thin films were examined from EDX, as shown in Fig. 17. The 30-nm-thick sample has a 94.56 at% and 5.44 at% of In and Se in the film, respectively. The volatilization of Se occurred and the chemical composition of Se decreased to fewer with the RTA process above 600°C [39].

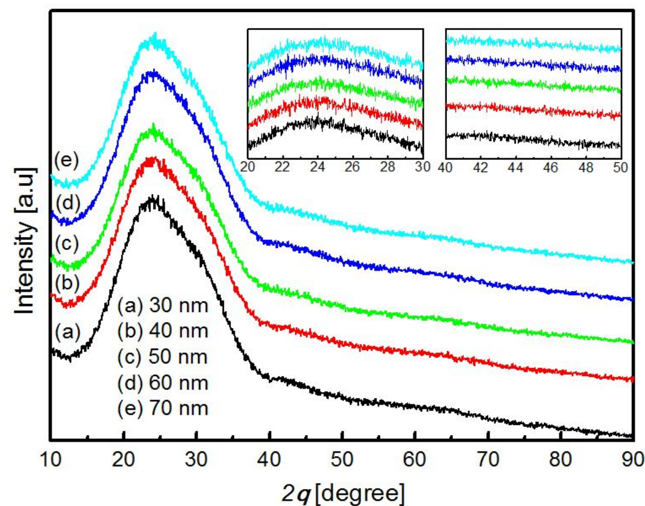

Fig. 16 XRD spectra of the indium selenide thin films at the different thickness of (a) 30, (b) 40, (c) 50, (d) 60, and (e) 70 nm

Collection @ chosun

조선대학교 CHOSUN UNIVERSITY

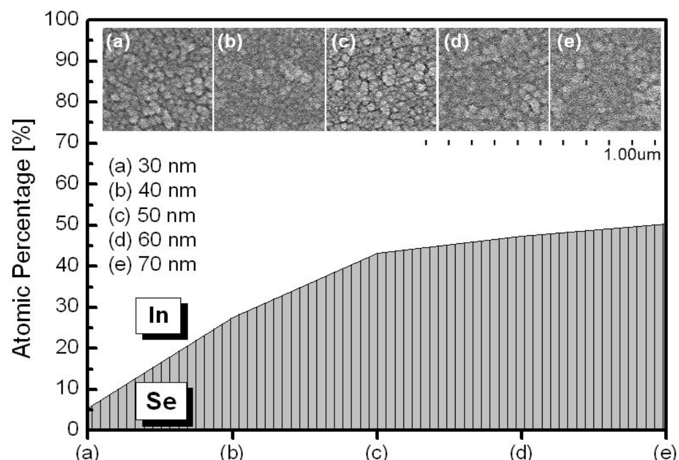

Fig. 17 FESEM images and atomic percent of the indium selenide thin films at the different thickness of (a) 30, (b) 40, (c) 50, (d) 60, and (e) 70 nm

The chemical composition of Se was very few when the $InSe_2$ target was used and RTA treatment was performed at 700°C. The chemical composition of Se increased with an increase in the film thickness from (a) 30 to (e) 70 nm. Se of 50.28 at% in the film overtook In of 49.72 at% in the 70-nm-thick sample. Indium selenide is one of the layered compounds which have individual crystal planes loosely bound to each layer by weak Van der Waals force. Bulky crystals in thinner film are easily cleavable in their layered planes because Se is more volatile than In in the Se-In interlayer bonds [23]. The calculated molar ratios of In to Se were 11.954, 1.799, 0.906, 0.767, and 0.680 in RTA-treated indium selenide thin films at the film thickness of (a) 30, (b) 40, (c) 50, (d) 60, and (e) 70 nm, respectively. These molar ratios were nonstoichiometries approaching the stoichiometric compositions of $In_{12}Se$, In_9Se_5, In_9Se_{10}, In_3Se_4, and In_2Se_3 in the amorphous indium selenide thin films, respectively.

Indium selenides in amorphous nature exhibit unusual properties compared with other chalcogenides [36], influences of the different chemical composition with a change of film thickness should be studied on electrical

Collection @ chosun

조선대학교 CHOSUN UNIVERSITY

and optical properties of the amorphous indium selenides. Figure 18 shows the optical transmittance in the visible to near-infrared (NIR) spectral region (300–1800 nm) of the different-thickness indium selenide thin films. All transmittance spectra show no interference pattern against the prior lituratures especially without an abrupt increase in spectrum at 560 or 640 nm caused by the phase transition from In_xSe_y to γ-In_2Se_3 [13,24,25,40]. The absorption edge in the optical transmittance shifted towards the shorter wavelengths (or the suitable property as a buffer layer in CIGS solar cells) with a decrease in the film thickness. Mean optical transmittance of indium selenide thin films with all thickness ≤ 70 nm showed the very high values ≥ 87% in the visible spectral region (400–800 nm), as shown in the inset of Fig. 18.

Mean optical transmittance improved from 87.63% to 96.03% as decreasing film thickness from 70 to 30 nm. In the visible to NIR spectral region (400–1600 nm), the mean optical transmittance also showed the similar tendency to increase with a decrease in film thickness while the values were somewhat higher values of 88.33 to 96.42 % than those in the range from 400 to 800 nm, respectively.

Band gap energies of the indium selenide thin films were estimated by linearly extrapolating each curve back to the energy axis of the plot of $(\alpha h\upsilon)^2$ vs. the $h\upsilon$ (Tauc plot), where α is the absorption coefficient, h is Planck's constant (4.135667×10^{-15}eVs), and υ is the frequency of the incident photon. Individual band gap energies of the indium selenide thin films with the different film thickness of (a) 30, (b) 40, (c) 50, (d) 60, and (e) 70 nm were 3.048, 2.949, 2.940, 2.925, and 2.875 eV, as shown in the inset of Fig. 19, respectively, which showed that E_g is inversely proportional to the film thickness of indium selenides in amorphous nature [24]. The increased E_g allows the transmission of more incident-light at shorter wavelengths, which agrees with the shift of absorption edge in Fig. 18. All E_g were suitable for the buffer layer in the proper range between CIGS and transparent conductive oxide (1.68 eV ≤ E_g ≤ 3.4 eV), even though the values of E_g in amorphous nature were greater that the well-known values in the crystalline indium

Collection @ chosun

조선대학교 CHOSUN UNIVERSITY

selenides due to the higher energy for the electron transitions between localized and extended states at valence/conduction band in amorphous materials [24,25].

Some electrical properties, such as the resistivity, carrier concentration, carrier mobility, and conductivity type, of the indium selenide thin films were examined by Hall Effect measurements with a change of the film thickness, as shown in Fig. 20. It is well known that most amorphous chalcogenides are p-type conductivity. Carrier concentration of the indium selenide thin films, showing p-type conductivity, was in the $10^{15}cm^{-3}$-order-of-magnitude of excessive holes at the film thickness of 50 nm with the chemical composition of In ~ 57 at%. The carrier concentration was abruptly changed with an increase in the film thickness ≤ 40 nm (i.e., at the chemical composition of In ≥ 72 at%), which showed 10^{15}–$10^{16}cm^{-3}$-ordered n-type conductivity of excessive electrons in the specimen. Similar results could be observed in the prior studies revealing the conductivity of indium selenides became n-type from p-type for high In concentration ≥ 60 at%, which was caused by increase in number of crystallites (atomic arrangements) with n-type conductivity with an increase in indium concentration in the amorphous indium selenides [10,23]. The carrier concentration also showed 10^{15}–$10^{16}cm^{-3}$-ordered n-type conductivity of excessive electrons in the indium selenides with a decrease in the film thickness ≥ 60 nm corresponding to the chemical composition of In ~ 50 at%.

Carrier mobility decreased with increasing the film thickness from (a) 30 to (b) 40 nm due to the rapidly decrease in the chemical composition of In, because the dissolved In in the Se chains tends to bind Se to increase the length of amorphous short-range order as increasing In concentration [6,35]. Carrier mobility increased with an increase in the film thickness from (c) 50 nm because the decreased electron scattering contributes to further increase in carrier mobility in amorphous nature as increasing the film thickness whereas the chemical composition of In gradually decreased from (c) 50 nm [18].

Collection @ chosun

조선대학교
CHOSUN UNIVERSITY

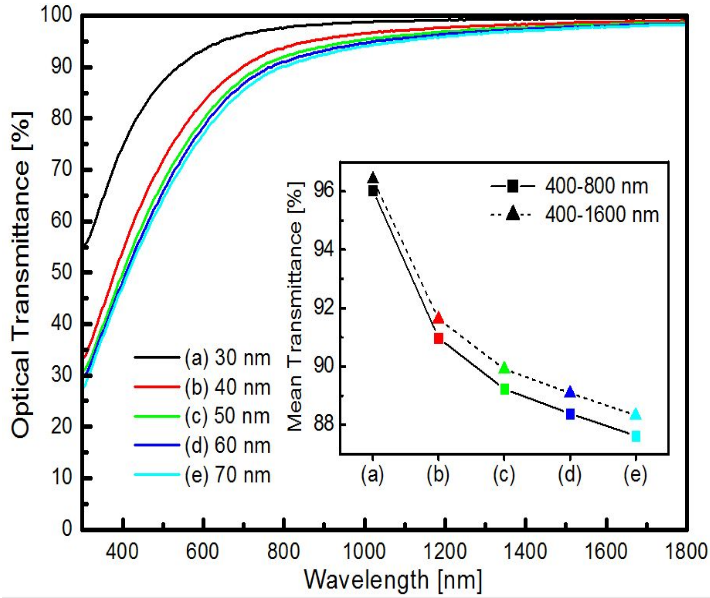

Fig. 18 Optical transmittance of the indium selenide thin films at the different thickness of (a) 30, (b) 40, (c) 50, (d) 60, and (e) 70 nm

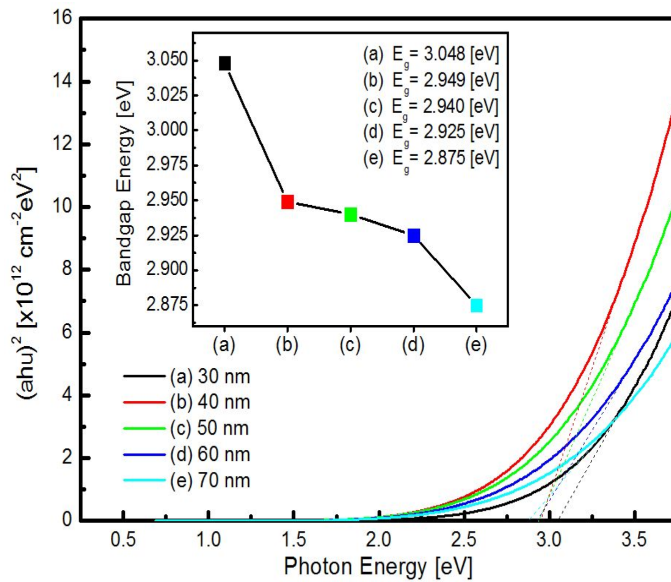

Fig. 19 Band gap energy of the indium selenide thin films at the different thickness of (a) 30, (b) 40, (c) 50, (d) 60, and (e) 70 nm

Collection @ chosun

조선대학교 CHOSUN UNIVERSITY

Resistivity of the different-thickness indium selenides in amorphous nature has the range of 10^3–10^4Ω·cm–orders-of-magnitude lower than that of the γ-In_2Se_3, which is also superior to the reported values (10^3–10^{11}Ω·cm) of CdS thin films as the conventional buffer layer for CIGS thin film solar cells [15,16]. The resistivity generally depends on the carrier concentration and carrier mobility as well as is usually in inverse proportion to the film thickness at the similar composition. However, the resistivity of the indium selenides showed the increased tendency with an increase in the film thickness. The transition behaviour in conductivity might be proceeding partly with a poor conductive p-type in a conductive n-type at the film thickness of (b) 40 and (d) 60 nm corresponding to the chemical composition of In from 72.35 to 52.72 at%, respectively [41]. The main attribution to the slightly decrease in the resistivity at the film thickness of (e) 70 nm was caused by the rapidly increase in carrier mobility of the excessive electrons with n-type conductivity in the specimen.

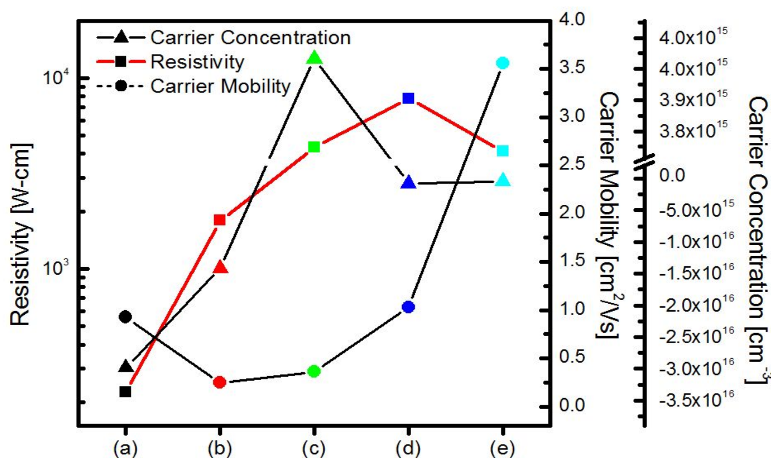

Fig. 20 Resistivity, carrier Concentration and carrier mobility of the indium selenide thin films at the different thickness of (a) 30, (b) 40, (c) 50, (d) 60, and (e) 70 nm

Collection @ chosun

조선대학교
CHOSUN UNIVERSITY

VI. Conclusion

Amorphous indium selenide thin films as a buffer layer for CIGS solar cells were prepared using a RF magnetron sputtering with $InSe_2$ target. RTA was used to control the non-stoichiometric Se-concentration in the indium selenides because Se is very volatile in high-temperature heat treatment. Chemical composition ratio of Se to In decreased with increasing the annealing temperature from 400°C to 700°C. However, the indium selenide thin films of ~50-nm-thickness remained amorphous phase regardless of the thermal treatment at the annealing temperature ≤ 700°C. Optical transmittance was improved to 75.33% and band gap energies increased from 2.451 to 3.085eV with increasing the annealing temperature (*i.e.*, with decreasing the chemical composition of Se). All band gap energies were good and able to be controlled for the buffer layer in CIGS thin film solar cells. Resistivity decreased to the order-of-magnitude from 10^4 to 10^1Ω-cm as an increase in the annealing temperature, which were enough to replace the conventional CdS buffer layer. Carrier concentration increased rapidly to the order-of-magnitude of $10^{17}cm^{-3}$ and conductivity was changed abruptly from p-type to n-type in the remained amorphous nature at the lower Se concentration.

Indium selenide thin films were prepared with different thickness of 30–70 nm using a RF magnetron sputtering with $InSe_2$ target and RTA treatment at 700°C as a buffer layer for CIGS solar cells. Chemical composition of the indium selenide thin films was changed with increasing the film thickness in amorphous nature. Optical transmittance was improved from 87.63% to 96.03% and E_g decreased from 3.048 to 2.875 eV as decreasing the film thickness. Conductivity type of the amorphous indium selenide thin films showed n-type at the film thickness at ≤ 40 or ≥ 60 nm-thickness (≤ 52.72 or ≥ 72.35 at%-composition of In) except a p-type at 50 nm (56.85 at%). Carrier concentration and resistivity of the different-thickness indium selenide

Collection @ chosun

조선대학교 CHOSUN UNIVERSITY

thin films in amorphous nature has the range of 10^{15}–$10^{16}cm^{-3}$ and 10^{3}–$10^{4}\Omega\cdot cm$ orders-of-magnitude, respectively. Optical and electrical properties of indium selenide thin films in amorphous nature could be tunable with the film thickness induced the chemical composition ratio, these properties were even better than those of the γ-In_2Se_3 and enough to replace the CdS thin films as a conventional buffer layer in CIGS solar cells.

Collection @ chosun

조선대학교 CHOSUN UNIVERSITY

Reference

[1] B. T. Jheng, P. T. Liu, M. C. Wu and H. P. D. Shieh, Opt. Lett., 37 (2012) 2760.

[2] Y. C. Lin, J. H. Ke and C. C. Chen, Appl. Mech. Mater., 189 (2012) 63.

[3] G. Gordillo and C. Calderón, Sol. Energy Mater. Sol. Cells, 77 (2003) 163.

[4] M. J. Kim, and S. H. Lee, *J. Nanoelectron. Optoe.*, 9 (2014) 57.

[5] A. A. A. Darwisha, M. M. El-Nahassc, and M. H. Bahlold, *Appl. Surf. Sci.*, 276 (2013) 210.

[6] R. E. Ornelas, D. Avellaneda, S. Shaji, G. A. Castillo, T. K. Das Roy and B. Krishnan, Appl. Surf. Sci., 258 (2012) 5753.

[7] Y. Ohtake, T. Okamoto, A. Yamada, M. Konagai and K. Saito, Sol. Energy Mater. Sol. Cells, 49 (1997) 269.

[8] M. L. Madugu, L. Bowen, O. K. Echendu, and I. M. Dharmadasa, *J. Mater. Sci: Mater. Electron*, 25 (2014) 3977.

[9] H. Okamoto, J. Phase Equilib. Diff., 25 (2004) 201.

[10] M. Parlak, and C. Ercelebi, *Thin Solid Films*, 322 (1998) 334.

[11] A. Ates, M. Kundakçı, A. Astam, and M. Yıldırım, *Physica E*, 40 (2008) 2709.

[12] R. Sreekumar, T. H. Sajeesh, T. Abe, Y. Kashiwaba, C. S. Kartha, and K. P. Vijayakumar, *Phys. Status Solidi B*, 250 (2013) 95.

[13] S. Li, Y. Yan, Y. Zhang, Y. Ou, Y. Ji, L. Liu, C. Yan, Y. Zhao, and Z. Yu, *Vacuum*, 99 (2014) 228.

[14] K. Ellmer, A. Klein and B. Rech, Transparent Conductive Zinc Oxide Basics and Applications in Thin Film Solar Cells, Springer-Verlag, Berlin, Heidelberg, 2008 ed., 2008, p. 6.

[15] P. Roy and S. K. Srivastava, Mate. Chem. Phys., 95 (2006) 235.

[16] J. H. Yoon, W. M. Kim, J. K. Park, Y. J. Baik, T. Y. Seong and J. Jeong, Prog. Photovolt: Res. Appl., 22 (2014) 69.

Collection @ chosun

조선대학교 CHOSUN UNIVERSITY

[17] C. Viswanathan, S. Gopal, D. Mangalaraj, Sa. K. Narayandass, O. F. Caltun, G. Rusu, and Junsin Yi, *Ionics*, 10 (2004) 311.
[18] H.-D Liu, Y.-P Zhao, G Ramanath, S.P Murarka, and G.-C Wang, *Thin Solid Films*, 384 (2001) 151.
[19] K. Bouabid, A. Ihlal, A. Manar, A. Outzourhit and E. L. Ameziane, Thin Solid Films, 488 (2005) 62.
[20] E. Ahmed, A. Zegadi, A. E. Hill, R. D. Pilkington, R. D. Tomlinson, A. A. Dost, W. Ahmed, S. Leppävuori, J. Levoska and O. Kusmartseva, J. Mater. Sci: Mater. Electron, 7 (1996) 213.
[21] N. H. Kim, Y. K. Jun and G. B. Cho, J. Electr. Eng. Technol., 9 (2014) 1009.
[22] X. Wang, S. S. Li, W. K. Kim, S. Yoon, V. Craciun, J. M. Howard, S. Easwaran, O. Manasreh, O. D. Crisalle and T. J. Anderson, Sol. Energy Mater. Sol. Cells, 90 (2006) 2855.
[23] F. S. Terra, G. M. Mahmoud, L. Mourad, and A. Tawfik, Indian J. Phys., 86 (2012) 1093.
[24] J. Hossain, M. Julkarnain, K. S. Sharif, and K. A. Khan, *Int. J. Renewable Ener.*, 2 (2013) 220.
[25] A. Mohan, J. Suthagar, and T. Mahalingam, Investigation on the Structural and Optical Properties of Thermally Evaporated Indium Selenide Compound Material for Solar Cell Application, Proceedings of the International Conference Nanomaterials: Applications and Properties, Vol. 2 No 1, 01NTF07 (2013) 5.
[27] D. Rudmann, A.F. da Cunha, M. Kaelin, F. Kurdesau, H. Zogg, A.N. Tiwari, G. Bilger, Appl. Phys. Lett. 84 (2004) 1129.
[28] Contreras, M.A., Tuttle, J,Gabor, A.Tennant, A.Ramanathan, K.Asher, S.Franz, A.Keane, J.Wang, L.Scofield, J. Noufi, R., 1st WCPEC. (1994) 68.
[29] L. Stolt, J. Hedstrom, J. Skarp, 1st WCPEC. (1994) 250.
[30] D. Rudmann, Ph. D. thesis, University of Basel (2004).
[31] D. Souri and K. Shomalian, J. Non-Cryst. Solids 355, (2009) 1597.

Collection @ chosun

조선대학교 CHOSUN UNIVERSITY

[32] J. M. González-Leal, A. Ledesma, A. M. Bernal-Oliva, R. Prieto-Alcón, E. Márquez, J. A. Angel and J. Cárabe, Mater. Lett. 39, (1999) 232.
[33] N. H. Kim, C. I. Park, J. Park, J. Korean Phys. Soc. 62, (2013) 502.
[34] J. M. P. Coelho, M. A. Abreu and F. C. Rodrigues, Polym. Test. 23, (2004) 307.
[35] F. I. Mustafa, S. Gupta, N. Goyal and S. K. Tripathi, Physica B, 405 (2010) 4087.
[36] K. Bindu, M. Lakshmi, S. Bini, C.S. Kartha, K.P. Vijaykumar, T. Abe and Y. Kashiwaba, Semicond. Sci. Technol., 17 (2002) 270.
[37] J. C. Bernède, S. Marsillac, A. Conan and A. Gody, J. Phys: Condens. Matter, 8 (1996) 3439.
[38] K. Lu, M. L. Sui, J. H. Perepezko and B. Lanning, J. Mater. Res., 14 (1999) 771.
[39] M. H. Yoo, Y. S. Park, and N. H. Kim, *J. Nanosci. Nanotechno.*, *In Review* (2014).
[40] Y. Yan, S. Li, Y. Ou, Y. Ji, L. Liu, C. Yan, Y. Zhang, Z. Yu, and Y. Zhao, *J. Alloy. Compd.*, 614 (2014) 368.
[41] S. Marsillac, J. C. Bernéde, and A. Conan, *J. Mater. Sci.* 31, (1996) 581.

Collection @ chosun